The Lagrangian Atmospheric Radionuclide Transport Model (ARTM) — development, description and sensitivity analysis

Robert Hanfland[1,5] · Margit Pattantyús-Ábrahám[1] · Cornelia Richter[2] · Dominik Brunner[3] · Christiane Voigt[4,5]

Abstract

Atmospheric dispersion models are applied to describe and predict the dispersion of emitted plumes. Here, we describe the Lagrangian Atmospheric Radionuclide Transport Model (ARTM) 2.8.0 which was developed to simulate the atmospheric dispersion of the emissions of nuclear facilities under routine operation for regulatory purposes over annual time scales. ARTM includes a diagnostic wind field model and a particle dispersion model. It simulates size-dependent wet and dry deposition, plume rise and γ-cloud shine of radioactive exhaust plumes in the simulation domain. This work presents an extensive overview of the different components of the model and of the physical and mathematical concepts of ARTM. We investigate the dependence of the plume dispersion in terms of plume volume, position of maximum concentration and dry deposition rates on key input parameters such as atmospheric stability, surface roughness, zero plane displacement height, source height and the particle size in the case of particulate matter tracers. The results indicate a strong dependence of plume volume and position of the maximum concentration on the stability as well as a minor influence on surface roughness. The source height above ground level has a low impact on the plume volume as the zero plane displacement only slightly affects the position of maximum concentration. Strong turbulence under unstable conditions tends to reduce the impact of sedimentation and decreases deposition in general. This computational model serves to advance the understanding of the dispersion of radioactive plumes in the boundary layer.

Keywords ARTM · Lagrangian particle dispersion model · Model description · Local sensitivity analysis

✉ Margit Pattantyús-Ábrahám
mpattantyus@bfs.de

Robert Hanfland
rhanfland@bfs.de

Dominik Brunner
dominik.brunner@empa.ch

1 Department Radiation Protection and Environment, Bundesamt für Strahlenschutz, Oberschleißheim, Germany

2 Radiation and Environmental Protection Department, Gesellschaft für Anlagen- und Reaktorsicherheit (GRS) gGmbH, Köln, Germany

3 Air Pollution/Environmental Technology, Empa Swiss Federal Laboratories for Material Science and Technology, Dübendorf, Switzerland

4 Institute of Atmospheric Physics, Deutsches Zentrum für Luft- und Raumfahrt, Oberpfaffenhofen, Germany

5 Institute of Atmospheric Physics, Johannes Gutenberg-Universität Mainz, Mainz, Germany

Introduction

Lagrangian particle dispersion models (LPDMs) are a common tool for modelling the dispersion of tracers in the atmosphere. In such models, the real tracers are represented by numerical particles which are propagated in space and time with respect to a flow and turbulence field forming distinguishable trajectories for each numerical particle, respectively (Leelőssy et al. 2014). Therefore, Lagrangian models such as MSS/PMSS (Moussafir et al. 2004; Oldrini et al. 2017), FLEXPART (Stohl et al. 2005), HYSPLIT (Stein et al. 2015), PALM (Maronga et al. 2015) or NAME (Maryon et al. 1991) are more realistic compared to Gaussian models. LPDMs are more and more often used for regulatory, safety or authorization purposes especially when the tracers are potentially harmful to the public such as emissions from nuclear facilities (Simmonds et al. 1995; Walter 2004; Leelőssy et al. 2014). Exposure caused by airborne effluents of such facilities is difficult to access experimentally. Under routine operation, radioactive exposure from nuclear facilities

can not be distinguished from the natural background radiation in the surrounding of the issuer (Lee et al. 2019). Therefore, the additional exposure to the public originating from nuclear facilities is often assessed using atmospheric dispersion models (Mayall 2003; StrlSchV 2018; AVV 2012; AVV Tätigkeiten 2020).

In Germany, the supervision of nuclear facilities including the monitoring of the immissions of the exhaust plume is controlled by regulations which also give guidelines for the dispersion modelling (AVV 2012; StrlSchV 2018; AVV Tätigkeiten 2020).

The Atmospheric Radionuclide Transport Model (ARTM) was developed by the Gesellschaft für Anlagen- und Reaktorsicherheit (GRS) gGmbH on behalf of the Federal Office for Radiation Protection (BfS) in 2007. It is designed for the purpose of modelling the annual atmospheric dispersion of radioactive substances from nuclear facilities under routine conditions in a radius of typically 10 km. It fulfils the requirements and guidelines of german authorities and is freely available (https://www.bfs.de/EN/topics/ion/environment/air-soil/emission-monitoring/artm.html). Due to its specific field of application, it is designed to run on common desktop computers and requires low computational costs compared to more complex models such as large eddy simulations (LES), computational fluid dynamic (CFD) models or models which include prognostic wind field simulations.

ARTM consists of the diagnostic wind field model TALdia and a particle model to propagate radioactive particles in space and time. It is based on the model AUSTAL2000 (Janicke and Janicke 2003) version 2.2.11 which was developed for conventional tracers (GRS 2007).

In this work we present the first extensive model description of ARTM version 2.8.0 in a scientific publication including the wind field model TALdia, the particle transport model and the features to tackle with radionuclides such as dry and wet deposition or radioactive decay. Some features of the model, such as the handling of buildings in the flow field or the plume rise through cooling towers are beyond the scope of this work and are therefore excluded from this description.

However, verification and validation of a model have to be part of any development process in order to assure reliability (Kleijnen 1995). In addition, sensitivity analyses can guide future research and application efforts (Hamby 1994). Sensitivity analyses can give information about the input parameters and their influence on the simulation results which is important for the operational use of a model (Rao 2005).

During the development process, ARTM has been verified and validated within several test cases for activity concentrations at the ground (GRS 2007; Martens et al. 2012; Hettrich 2017) and it had been compared with a Gaussian plume model (Richter 2016). Furthermore, a scenario-based sensitivity analysis of some input parameters

(e.g. emission rate, source geometry, roughness length and particle number) had been performed by Hettrich (2017). However, this analysis only dealt with the influence on the activity concentration at the ground level at some selected observation points.

In this work a local sensitivity analysis of the input parameters assumed to be most influencing to dispersion of the exhaust plume such as the diffusion category (DC), the roughness length, the zero plane displacement and the source height above ground level (AGL) is performed. The analysis is not limited to the ground level concentration but investigates the three-dimensional structure of the simulated plume. Furthermore, the effect of the particle size of the tracers on the deposition distribution is analysed. In order to focus on the dispersion properties of ARTM a general simulation setup without orography or obstacles is used.

The wind field model TALdia

The diagnostic wind field model TALdia was developed by Janicke Consulting and provides wind and turbulence fields for the Lagrangian particle dispersion model ARTM when terrain is present (Janicke and Janicke 2003, 2004; GRS 2007). TALdia uses a mass conservation approach to model the wind field within the simulation domain. Hourly wind fields are generated by using a boundary layer model and in-situ measured wind $\vec{v}_{\text{meas}}$ (velocity and direction) at a single location within the simulation domain (Richter et al. 2015b). In the absence of terrain, only the boundary layer model described in the next section is applied to model the wind and turbulence fields. In this work TALdia 2.7.0 is described.

The boundary layer model of TALdia

The boundary layer model is based on similarity theory and employs a logarithmic wind profile where the mean wind speed $|\overline{\vec{v}(z)}|$ at height z depends on the atmospheric stability as

$$|\overline{\vec{v}(z)}| = \frac{u_*}{\kappa} \cdot$$

$$
\begin{cases}
\left\{ \ln\left[\dfrac{(\psi-1)(\psi_0+1)}{(\psi+1)(\psi_0-1)}\right] \right. \\
\qquad \left. +2\left(\tan^{-1}\psi - \tan^{-1}\psi_0\right) \right\} & \text{for } \dfrac{z'}{L} < 0 \\[4pt]
\left\{ \ln\dfrac{z'}{z_0} + 5\left(\dfrac{z'-z_0}{L}\right) \right\} & \text{for } 0 \le \dfrac{z'}{L} < 0.5 \\[4pt]
\left\{ 8\ln\left(2\dfrac{z'}{L}\right) + 4.25\left(\dfrac{z'}{L}\right)^{-1} - 0.5\left(\dfrac{z'}{L}\right)^{-2} \right. \\
\qquad \left. -\ln\left(2\dfrac{z_0}{L}\right) - 5\dfrac{z_0}{L} - 4 \right\} & \text{for } 0.5 \le \dfrac{z'}{L} < 10 \\[4pt]
\left\{ 0.7585\dfrac{z'}{L} + 8\ln 20 - 11.165 - \ln\left(2\dfrac{z_0}{L}\right) - 5\dfrac{z_0}{L} \right\} & \text{for } 10 \le \dfrac{z'}{L}
\end{cases}
$$

(1)

with

$$z' = z - d_0, \tag{2a}$$

$$\psi = \left(1 - 15\frac{z' + z_0}{L}\right)^{\frac{1}{4}} \tag{2b}$$

and

$$\psi_0 = \left(1 - 15\frac{z_0}{L}\right)^{\frac{1}{4}} \tag{2c}$$

where L is the Obukhov length, u_* is the friction velocity, $\kappa = 0.4$ is the von Kármán constant, z_0 denotes the roughness length (VDI 3783 part 8 2002; Lamb et al. 1979) and d_0 represents the zero plane displacement (Stull 1988). The Obukhov length is either determined directly from measurements or by determining the atmospheric stratification and dividing its stability into six diffusion categories parametrizing the turbulence in the atmosphere (Klug 1969; Richter et al. 2015a). In the latter case, the Obukhov length can be determined using the DC and the roughness length according to Table 1. The profile below $z = d_0 + 6 \cdot z_0$ follows a linear profile down to the surface with $|\vec{v}(z = 0)| = 0$. The transition from logarithmic to linear profile is continuous (TA Luft 2002).

For the determination of the friction velocity, Eq. 1 is evaluated at the height of the measurement data $z = z_{\text{meas}}$ using $u_* = 1\,\text{m}\,\text{s}^{-1}$. The resulting wind speed at the height of the measurement data is denoted with $|\vec{v}(z_{\text{meas}})|_{u_*=1\,\text{m}\,\text{s}^{-1}}$. The friction velocity can be seen as a proportional factor between the obtained wind speed at the height of the measurement data and the measured wind speed $|\vec{v}_{\text{meas}}|$ and is given by

$$u_* = \frac{|\vec{v}_{\text{meas}}|}{|\vec{v}(z_{\text{meas}})|_{u_*=1\,\text{m}\,\text{s}^{-1}}} \cdot 1\,\text{m}\,\text{s}^{-1} \tag{3}$$

(Janicke 2015).

The mixing layer top h_{m} is assumed to be equal to the boundary layer top and depends on the atmospheric stability (Richter et al. 2015a; VDI 3783 part 8 2002). For unstable atmospheric conditions, a mixing layer depth of 1100 m is used (TA Luft 2002). For all other conditions

$$h_{\text{m}} = \min(H_{\text{m}}, 800\,\text{m}) \tag{4}$$

is valid, where

$$H_{\text{m}} = 0.3\frac{u_*}{f_{\text{c}}}\begin{cases} 1 & \text{for } L \geq \dfrac{u_*}{f_{\text{c}}} \\ \left(\dfrac{f_{\text{c}}L}{u_*}\right)^{\frac{1}{2}} & \text{for } 0 < L < \dfrac{u_*}{f_{\text{c}}} \end{cases} \tag{5}$$

and f_{c} denotes the Coriolis parameter (TA Luft 2002; Seinfeld 1986).

The wind direction $d(z)$ within the boundary layer is assumed to change with height AGL according to an Ekman spiral and is given as

$$d(z) = d_{\text{meas}} + D(z) - D(z_{\text{meas}}) \tag{6}$$

with

$$D(z) = 1.23 \cdot D_{\text{h}} \cdot \left[1 - \exp\left(-1.75\frac{z}{h_{\text{m}}}\right)\right] \tag{7}$$

where D_{h} depends on the Obukhov length as

$$D_{\text{h}} = \begin{cases} 0° & \text{for } \dfrac{h_{\text{m}}}{L} < -10 \\ 45° + 4.5\dfrac{h_{\text{m}}}{L} & \text{for } -10 \leq \dfrac{h_{\text{m}}}{L} < 0 \\ 45° & \text{for } L > 0 \end{cases} \tag{8}$$

and d_{meas} is the wind direction of the measurement data (TA Luft 2002).

Using the mixing layer depth h_{m} and the friction velocity u_*, the standard deviation of wind fluctuation σ, the Lagrangian time scale T_{L} and the diffusion coefficient K are calculated for each component of the wind vector. The components are defined according to the downwind

Table 1 Scheme for the determination of the Obukhov length in metre from DC and roughness length as it is used by ARTM. After Richter et al. (2015a)

| Roughness length z_0 (m) | Diffusion category | | | | | |
	I very stable	II stable	III$_1$ neutral	III$_2$ indifferent	IV unstable	V very unstable
0.01	7	25	99999	−25	−10	−4
0.02	9	31	99999	−32	−13	−5
0.05	13	44	99999	−45	−19	−7
0.10	17	60	99999	−60	−25	−10
0.20	24	83	99999	−81	−34	−14
0.50	40	139	99999	−130	−55	−22
1.00	65	223	99999	−196	−83	−34
1.50	90	310	99999	−260	−110	−45
2.00	118	406	99999	−326	−137	−56

direction and denoted as medial (m), lateral (l) and vertical (v). The components of the wind fluctuation are

$$\sigma_m(z) = \begin{cases} 2.4u_* \left(1 + 0.01486\dfrac{-h_m}{\kappa L}\right)^{\frac{1}{3}} \exp\left(\dfrac{-z}{h_m}\right) & \text{for } L < 0 \\ 2.4u_* \exp\left(\dfrac{-z}{h_m}\right) & \text{for } L > 0 \end{cases}$$

(9a)

$$\sigma_l(z) = \begin{cases} 1.8u_* \left(1 + 0.03522\dfrac{-h_m}{\kappa L}\right)^{\frac{1}{3}} \exp\left(\dfrac{-z}{h_m}\right) & \text{for } L < 0 \\ 1.8u_* \exp\left(\dfrac{-z}{h_m}\right) & \text{for } L > 0 \end{cases}$$

(9b)

$$\sigma_v(z) = \begin{cases} 1.3u_* \left[\left(1 - 0.8\dfrac{z}{h_m}\right)^3 \dfrac{-z}{\kappa L} + \exp\left(\dfrac{-z}{h_m}\right)^3\right]^{\frac{1}{3}} & \text{for } L < 0 \\ 1.3u_* \exp\left(\dfrac{-z}{h_m}\right) & \text{for } L > 0 \end{cases}$$

(9c)

for a given grid cell point (VDI 3783 part 8 2002).

The components of the Lagrangian time scale are parametrized according to

$$T_{Li} = \frac{2\Sigma_i}{C_0 \eta} \tag{10}$$

where $\Sigma_i = \sigma_i^2$ is the variance of the wind fluctuation, i indicates the coordinate ($i = m, l, v$), C_0 denotes the Kolmogorov constant and is assumed to be $C_0 = 5.7$ and η is the dissipation rate of turbulent kinetic energy. Depending on the atmospheric stability, η can be determined empirically (VDI 3783 part 8 2002). For unstable and neutral stratification it can be given as

$$\eta = \max\left\{\frac{u_*^3}{\kappa z}\left[\left(1 - \frac{z}{h_m}\right)^2 + \frac{z}{h_m}\right] \right.$$
$$\left. + \frac{-u_*^3}{\kappa L}\left[1.5 - 1.3\left(\frac{z}{h_m}\right)^{\frac{1}{3}}\right], \frac{u_*^3}{\kappa z}\right\} \tag{11}$$

while for stable stratification

$$\eta = \frac{u_*^3}{\kappa z}\left(1 + 4\frac{z}{L}\right) \tag{12}$$

holds.

The corresponding diffusion coefficients K_i are

$$K_i = \Sigma_i T_{Li}. \tag{13}$$

The tensors $\boldsymbol{\Sigma}(x)$, $\boldsymbol{K}(x)$ and $\boldsymbol{T}_L(x)$ are (3×3)-matrices constructed using the components Σ_i, K_i and T_{Li} for each grid cell, respectively.

Wind field modelling

In the initialization step $\mathfrak{I}$, an initial wind field is constructed from the measurement data $\vec{v}_{meas}$ (Ratto et al. 1994) according to the boundary layer model described above. The wind profile contains a logarithmic shape in the Prandtl layer (up to approximately 200 m). For wind flowing perpendicular to a mountain ridge, the wind velocity above the ridge increases. This leads to unrealistic large wind velocities at the ground of the mountain top. Janicke (2014) described this problem and ARTM uses a modification of the initial wind field by an additional profile $c(z)$ in order to overcome this artefact. The logarithmic shape of the wind profile in the Prandtl layer is removed by multiplying the initial wind field with c^{-1}. The profile $c(z)$ is given as

$$c(z) = \begin{cases} \dfrac{\ln(6)}{\ln\left(\dfrac{200\,\text{m}-d_0}{z_0}\right)} & \text{for } 0 < z < d_0 + 6z_0, \\[4mm] \dfrac{\ln\left(\dfrac{z-d_0}{z_0}\right)}{\ln\left(\dfrac{200\,\text{m}-d_0}{z_0}\right)} & \text{for } d_0 + 6z_0 < z \leq 200\,\text{m}, \\[4mm] 1 & \text{otherwise} \end{cases} \tag{14}$$

(Janicke 2015). The initial wind field and thus the modified initial wind field $\boldsymbol{V}_0$ do not necessarily fulfil the continuity equation which, assuming constant air density, is given as

$$\vec{\nabla} \cdot \vec{v} = \frac{\partial v_x}{\partial x} + \frac{\partial v_y}{\partial y} + \frac{\partial v_z}{\partial z} = 0 \tag{15}$$

(Ratto 1996). $\vec{v}$ denotes the wind vector while x, y and z are the coordinates in the Cartesian coordinate system.

In the adjustment step $\mathfrak{F}$, the initial wind field $\boldsymbol{V}_0$ is then optimized under the constraint of the continuity Eq. 15 to obtain the intermediate wind field $\boldsymbol{V}_{inter}$ (Janicke 2014; Ratto et al. 1994). For this purpose, the method presented by Sasaki (1958, 1970) is used where the functional

$$E(v_x, v_y, v_z) = \iiint \frac{1}{2}\left[a_h(v_x - v_x^0)^2 + a_h(v_y - v_y^0)^2 \right.$$
$$\left. + a_v(v_z - v_z^0)^2\right] dx\,dy\,dz \tag{16}$$

represents the deviation between the initial and the intermediate wind field (Ratto 1996). $v_{x,y,z}^0$ and $v_{x,y,z}$ are the wind components of the initial and the intermediate wind field, respectively, while a_h and a_v are the horizontal and vertical weighting factors or stability parameters and are termed "Gauss precision moduli" (Sasaki 1958; Sherman 1978). They are constant for the whole simulation domain. For the two horizontal directions identical Gauss precision moduli are assumed (Richter et al. 2015b). The aim is to minimize Eq. 16 under the constraint of mass conservation leading to the variational problem

$$\delta\left\{\iiint \frac{1}{2}\left[a_h(v_x - v_x^0)^2 + a_h(v_y - v_y^0)^2 + a_v(v_z - v_z^0)^2\right] dx\,dy\,dz + \right.$$
$$\left. \iiint \lambda\vec{\nabla} \cdot \vec{v}\,dx\,dy\,dz\right\} = 0 \tag{17}$$

where δ denotes the first variation and $\lambda = \lambda(x, y, z)$ is the Lagrange multiplier. The Euler-Lagrange equations

$$v_x = v_x^0 + \frac{1}{a_{\mathrm{h}}} \frac{\partial \lambda}{\partial x} \tag{18a}$$

$$v_y = v_y^0 + \frac{1}{a_{\mathrm{h}}} \frac{\partial \lambda}{\partial y} \tag{18b}$$

$$v_z = v_z^0 + \frac{1}{a_{\mathrm{v}}} \frac{\partial \lambda}{\partial z} \tag{18c}$$

give the solution of the variational problem of Eq. 17 (Ratto 1996). The substitution of the partial differentials of the continuity Eq. 15 with the Euler-Lagrange Eqs. 18 leads to an elliptical equation for λ as

$$\frac{\partial^2 \lambda}{\partial x^2} + \frac{\partial^2 \lambda}{\partial y^2} + \left(\frac{a_{\mathrm{h}}}{a_{\mathrm{v}}}\right) \frac{\partial^2 \lambda}{\partial z^2} = -a_{\mathrm{h}} \left(\frac{\partial v_x^0}{\partial x} + \frac{\partial v_y^0}{\partial y} + \frac{\partial v_z^0}{\partial z}\right) \tag{19}$$

which is then solved numerically using the Alternating-Directions Implicit (ADI) method (Press et al. 2002; Richter et al. 2015b). For solving Eq. 19 the boundary conditions described in "Boundary conditions" are used to ensure the resulting wind field to be free of divergence.

This resulting intermediate wind field V_{inter} is multiplied by the profile $c(z)$ of Eq. 14 to restore the previously removed logarithmic wind profile in the Prandtl layer. According to Janicke (2014), this workaround leads to lower and thus more realistic wind velocities at the ground of mountain ridges. The adjustment step $\mathfrak{F}$ is applied again to $c(z) \cdot V_{\mathrm{inter}}$ to obtain the divergence-free final wind field V (Janicke 2014).

Boundary conditions

In order to obtain a unique solution for the adjustment step $\mathfrak{F}$ (Eq. 17), boundary conditions for λ can be specified implicitly from Eq. 17 as

$$\lambda \, \delta \vec{v} \cdot \vec{n} = 0 \tag{20}$$

on the boundaries in x-, y- and z-direction where δ denotes the first variation normal to each boundary and $\vec{n}$ is the outward unit vector normal to the grid cell surface of the wind field (Sherman 1978; Ratto et al. 1994; Homicz 2002). A detailed derivation is given by Homicz (2002).

Equation 20 is only valid when either (i) $\lambda = 0$ or (ii) $\delta \vec{v} \cdot \vec{n} = 0$; if both terms (i) and (ii) are equal to zero there would be no unique solution (Sherman 1978):

(i) If $\lambda = 0$ is valid the variation of the normal wind component $\delta \vec{v} \cdot \vec{n}$ at the boundary is not zero. This implies an adjustment of the initial wind field in normal direction at the boundary, which means that there is a change of air mass entering or leaving the grid cell boundary. This is a "flow-through" boundary.

(ii) If the variation of the normal wind component is zero ($\delta \vec{v} \cdot \vec{n} = 0$), then there is no adjustment of the initial wind field at the boundary, which implies no air mass change through the boundary. This represents a "no-flow-through" boundary.

Flow-through boundaries are used for the lateral and the top border of the simulation domain while a no-flow-through boundary is used for the bottom of the simulation domain (Janicke and Janicke 2003).

Parametrization of atmospheric stability

The Gauss precision moduli a_{h} and a_{v} of Eq. 16 serve as an interface to get information about the atmospheric stability into the process of the wind field modelling (Sherman 1978) and to determine whether an obstacle is passed more likely in horizontal (flow around) or vertical (flow over) direction (Ratto 1996). Both Gauss precision moduli are connected as

$$a_{\mathrm{h}} = \frac{1}{a_{\mathrm{v}}} \tag{21}$$

where a_{v} is a function of the Strouhal number Str and defined as

$$a_{\mathrm{v}} = \frac{1}{2} Str^2 + \sqrt{1 + \frac{1}{4} Str^4}. \tag{22}$$

The Strouhal number Str is the product of the Brunt-Väisälä frequency N_{BV} and a characteristic time t_{c} as

$$Str = N_{\mathrm{BV}} \cdot t_{\mathrm{c}} \tag{23}$$

where

$$N_{\mathrm{BV}} = \sqrt{\frac{a_{\mathrm{g}}}{\theta} \frac{\mathrm{d}\theta}{\mathrm{d}z}} \tag{24}$$

and

$$t_{\mathrm{c}} = \frac{L_{\mathrm{c}}}{v_{\mathrm{c}}}. \tag{25}$$

a_{g} is the acceleration of gravity and θ is the potential temperature. In the case of unstable and very unstable conditions the potential temperature gradient $\frac{\mathrm{d}\theta}{\mathrm{d}z}$ is assumed zero leading to $a_{\mathrm{v}} = a_{\mathrm{h}} = 1$. For other stratifications $\frac{\mathrm{d}\theta}{\mathrm{d}z}$ is determined from the DC and the wind velocity after Nuclear Safety Standards Commission (KTA) (2017 Tab. 7-2). For the characteristic wind velocity $v_{\mathrm{c}} = v_{\mathrm{c}}(z)$, the wind profile of the initial wind field V_0 at the position of the measurement data is used (Janicke 2014). L_{c} is the geometric mean $L_{\mathrm{c}} = \sqrt{h_{\mathrm{c}} l_{\mathrm{c}}}$ of a characteristic height (height of a terrain structure) h_{c} and a characteristic length l_{c} given by

$$l_{\mathrm{c}} = \frac{h_{\mathrm{c}}}{2\gamma} \tag{26}$$

with the average slope within the simulation domain

$$\gamma^2 = \frac{\int \left(\frac{\partial b}{\partial x}\right)^2 + \left(\frac{\partial b}{\partial y}\right)^2 \mathrm{d}x \, \mathrm{d}y}{A_{\mathrm{domain}}}. \tag{27}$$

$b = b(x, y)$ is the terrain elevation and

$$A_{domain} = (x_{max} - x_{min})(y_{max} - y_{min}) \qquad (28)$$

is the area of the simulation domain where $x_{min/max}$ and $y_{min/max}$ represent the edges of the simulation domain in x- and y-direction. The characteristic height h_c is defined as

$$h_c = 4\sqrt{\frac{\int [b(x, y) - \bar{b}]^2 \, dx \, dy}{A_{domain}}} \qquad (29)$$

with the mean terrain elevation

$$\bar{b} = \frac{\int b(x, y) \, dx \, dy}{A_{domain}} \qquad (30)$$

(Janicke 2014).

Coordinate system

TALdia uses a height-based terrain-following σ-coordinate system initially presented by Gal-Chen and Somerville (1975). In the simulation domain the vertical coordinate z is zero at the bottom of the domain while the top of the simulation domain is denoted as $\hat{z} = const$ (Gal-Chen and Somerville 1975). Positions between the terrain surface b and the domain top $\hat{z}$ can be expressed as $h = z - b$. It is assumed that $\hat{z} \to \infty$ leading to $\hat{h} = \hat{z}$ (Janicke 2014). For the terrain-following coordinate system a new vertical coordinate s is introduced as

$$s(x, y) = \hat{h}(x, y) \cdot \sigma = \hat{h}(x, y) \cdot \frac{z(x, y) - b(x, y)}{\hat{z}(x, y) - b(x, y)} \qquad (31)$$

(Janicke 2014; Ratto 1996; Gal-Chen and Somerville 1975).

At the terrain surface $z(x, y) = b(x, y)$ is valid and thus the coordinate s is always zero at the surface. At the top of the domain $z(x, y) = \hat{z}(x, y)$ and therefore $s = \hat{h} = \hat{z}$ (Ratto et al. 1994; Janicke 2014). For the case of a flat surface (no terrain is present) the vertical coordinate remains unchanged $s = z$.

The vertical component of the wind speed is also transformed and used in ARTM. The vertical velocity v_s within the terrain-following coordinate system is obtained by differentiating Eq. 31 with respect to time leading to

$$v_s = v_z - \left(\frac{\partial b}{\partial x} v_x + \frac{\partial b}{\partial y} v_y\right) \qquad (32)$$

with the original vertical velocity v_z (Janicke 2014). A detailed derivation is given by Gal-Chen and Somerville (1975).

The particle dispersion model

The ARTM version 2.8.0 uses the particle dispersion model suggested by the Association of German Engineers (VDI) guideline 3945 part 3 in combination with VDI guideline

3782 part 3 for the plume rise (VDI 3945 part 3 2000; VDI 3782 part 3 1985; Richter et al. 2015a; Janicke 2014). The model also contains radionuclide specific features such as radioactive decay, dry and wet deposition and γ-cloud shine.

Advective and turbulent transport

The dispersion is modelled using numerical particles representing one or more real particles of one or more tracer species. For each small time step τ, the position of the numerical particles $\vec{x}_{new}$ is defined according to the 1st-order Euler forward integration scheme by

$$\vec{x}_{new} = \vec{x}_{old} + \tau \underbrace{\left[\vec{v}_{avg}(\vec{x}_{old}) + \vec{v}_{turb} + \vec{v}_{add} \right]}_{\vec{v}_{trans}} \qquad (33)$$

with the average velocity $\vec{v}_{avg}$ and the turbulent velocity $\vec{v}_{turb}$ representing the Reynolds decomposition of the wind vector (VDI 3945 part 3 2000; Mesinger and Arakawa 1976). $\vec{v}_{add}$ is an additional velocity vector representing, e.g., sedimentation or buoyancy, $\vec{v}_{trans}$ is denoted as the transport velocity and $\vec{x}_{old}$ is the former particle position. The time steps τ are small compared to the Lagrangian time scale and they are in the order of seconds to tens of seconds in practice.

$\vec{v}_{avg}$ is obtained by spacial interpolation from the final wind field V at the particle position (see "Wind field modelling") and is constant for the time $t = 1\,h$ while the turbulent velocity $\vec{v}_{turb}$ changes for each $\tau \ll t$ according to the Markov process

$$\vec{v}_{turb} = \mathbf{\Psi}(\vec{x}_{old}) \cdot \vec{v}_{turb,old} + \vec{W}(\vec{x}_{old}) + \mathbf{\Lambda}(\vec{x}_{old}) \cdot \vec{r} \qquad (34)$$

(VDI 3945 part 3 2000). $\mathbf{\Psi}$ is the autocorrelation tensor and given as

$$\mathbf{\Psi} \approx \mathbf{I} - \tau(\vec{x}) \left(\mathbf{\Sigma} \cdot \mathbf{K}^{-1} \right) \qquad (35)$$

with the identity matrix $\mathbf{I}$, $\vec{W}$ is the drift velocity

$$\vec{W} \approx \tau(\vec{x})\vec{\nabla} \cdot \mathbf{\Sigma}, \qquad (36)$$

$\mathbf{\Lambda}$ is the Cholesky decomposition of a tensor $\mathbf{\Omega}$ given as

$$\mathbf{\Omega} = \mathbf{\Lambda}\mathbf{\Lambda}^{\mathsf{T}} \approx \tau(\vec{x}) \left[\left(\mathbf{\Sigma} \cdot \mathbf{K}^{-1} \right) \cdot \mathbf{\Sigma} + \mathbf{\Sigma} \cdot \left(\mathbf{\Sigma} \cdot \mathbf{K}^{-1} \right)^{\mathsf{T}} \right] \qquad (37)$$

and $\vec{r}$ is a random vector with its components following a standard normal probability density distribution (Janicke 2000). The tensors $\mathbf{\Sigma}$ and K are obtained from the boundary layer model described in "The boundary layer model of TALdia".

Equations 35–37 are derived under the assumptions of (i) the additional velocity is zero ($\vec{v}_{add} = 0$); (ii) there are suitable boundary conditions to obtain a homogeneous steady-state particle distribution; (iii) in such

a homogeneous steady-state particle distribution the mean wind speed and its variance is equal to the mean particle velocity and its variance, respectively; (iv) at time scales much larger than the Lagrangian time scale a particle cloud spreads like the classic diffusion equation predicts; and (v) the small time steps $\tau(\vec{x})$ depend on the location. Using location-dependent time steps τ avoids very small time steps in the whole simulation domain and keeps the model computational efficient (VDI 3945 part 3 2000). A detailed derivation of Eqs. 35–37 is given by Janicke (2000).

Particle initialization and boundary conditions

All numerical particles start either at a point, line, area or volume source. In the latter cases the numerical particles are distributed randomly within the line, area or volume source. The initial turbulent velocity of each numerical particle is chosen randomly according to a standard normal distribution with its mean value $\overline{\vec{v}_{\text{turb}}} = \mathbf{\Sigma}(\vec{x})$ (VDI 3945 part 3 2000).

Particles crossing the upper and lateral boundaries of the simulation domain are erased from the simulation. At the terrain surface, numerical particles are elastically reflected instantaneously (with deposition for particulate matter (PM) as described in "Sedimentation, dry and wet deposition") and their turbulent velocity is changed to

$$\vec{v}_{\text{turb,new}} = \vec{v}_{\text{turb,old}} - 2(\vec{n} \cdot \vec{v}_{\text{turb,old}}) \cdot \vec{n} \tag{38}$$

(VDI 3945 part 3 2000).

The upper boundary of the mixing layer within the simulation domain can be crossed by the numerical particles. The atmosphere above the mixing layer is modelled as a region with no diffusion ($\vec{v}_{\text{turb}} = 0$) (VDI 3945 part 3 2000; GRS 2015).

Plume rise

Usually a rise of the plume relative to the emission height occurs due to buoyancy and inertia (Briggs 1971). In ARTM emissions are divided into two categories, emissions with heat content Q lower or higher than 1.4 MW. The heat Q in MW is calculated as

$$Q = c_{\text{p}} \cdot R_{\text{norm}} (T_{\text{e}} - 283.15\,\text{K}) \tag{39}$$

with $c_{\text{p}} = 1.36 \cdot 10^{-3}\,\text{MW s m}^{-3}\text{K}^{-1}$ being the specific heat capacity for the emissions of a pit coal fire, R_{norm} being the volume flux under standard conditions (temperature $T = 273.15\,\text{K}$ and pressure $p = 1013.25\,\text{hPa}$) and T_{e} being the temperature of the emissions (VDI 3782 part 3 1985).

For the first case ($Q \leq 1.4\,\text{MW}$), the momentum plays a significant role for the plume rise (VDI 3782 part 3 1985). Thus, according to Moses and Carson (1968) the maximum plume rise (relative to the height of the source AGL) is given

as

$$h_{\text{max}} = \max(h_{\text{b}}, h_{\text{i}}) \tag{40}$$

with

$$h_{\text{b}} = \left(0.35 \cdot v_{\text{emission}} \cdot d_{\text{source}} + 84 \cdot Q^{\frac{1}{2}}\right) |\vec{v}_h|^{-1} \tag{41}$$

and

$$h_{\text{i}} = 3 \cdot v_{\text{emission}} \cdot d_{\text{source}} \cdot |\vec{v}_h|^{-1}. \tag{42}$$

v_{emission} denotes the vertical velocity of the emission flux, d_{source} is the diameter of the source and $|\vec{v}_h|$ is the horizontal wind velocity in the height of the source taken from the final wind field V (GRS 2015). Equations 40–42 are valid for all turbulence conditions in the atmosphere (VDI 3782 part 3 1985).

The horizontal distance between the source and the maximum plume rise depends only on the heat Q and is given as

$$|\vec{x}_{h_{\text{max}}}| = 209.8 \cdot Q^{0.522}. \tag{43}$$

For the second case ($Q > 1.4\,\text{MW}$), the calculation depends on the turbulence in the atmosphere (VDI 3782 part 3 1985). Following Briggs, the horizontal distance from the source to the maximum plume rise is determined by

$$|\vec{x}_{h_{\text{max}}}| = \exp\left[\frac{\ln\left(\frac{h_{\text{max}} \cdot |\vec{v}_h|}{\alpha}\right) - \chi \ln Q}{q}\right] \tag{44}$$

(VDI 3782 part 3 1985; Briggs 1971). The empirical parameters α, χ and q depend on the atmospheric stability and the heat Q and are summarized in Table 2.

The maximum plume rise h_{max} for this case is calculated according to

$$h_{\text{max}} = \beta \cdot Q^{\epsilon} \cdot |\vec{v}_h|^{u} \tag{45}$$

with the empirical parameters β, ϵ and u given in Table 2 (Briggs 1971; VDI 3782 part 3 1985).

After the determination of h_{max} and $|\vec{x}_{h_{\text{max}}}|$ an additional vertical velocity $\vec{v}_{\text{pr}}$ for the numerical particles due to the plume rise is calculated as

$$\vec{v}_{\text{pr}} = \frac{h_{\text{max}}}{t_{\text{rise}}} \tag{46}$$

where

$$t_{\text{rise}} = 0.4 \cdot \frac{|\vec{x}_{h_{\text{max}}}|}{|\vec{v}_h|} \tag{47}$$

denotes the rise time. A numerical particle is assumed to move vertically with $\vec{v}_{\text{pr}}$ beginning from its release at the source until t_{rise} is reached (GRS 2015).

The given equations for the plume rise are only valid for emissions from sources with a vertical flux not influenced by obstacles. In the case of a wind speed at source height lower than $1\,\text{m s}^{-1}$ it is substituted with $|\vec{v}_h| = 1\,\text{m s}^{-1}$.

Table 2 Values of the parameters in Eqs. 44 and 45 for the different diffusion categories and heat contents Q. After VDI 3782 part 3 (1985)

	Diffusion category					
	I	II	III$_1$ + III$_2$		IV + V	
	$Q > 1.4$ MW		1.4 MW $< Q$ ≤ 6 MW	$Q > 6$ MW	1.4 MW $< Q$ ≤ 6 MW	$Q > 6$ MW
α	3.34	3.34	2.84	2.84	3.34	3.34
χ	0.333	0.333	0.333	0.333	0.333	0.333
q	0.667	0.667	0.667	0.667	0.667	0.667
β	74.4	85.2	78.4	102	112	146
ϵ	0.333	0.333	0.750	0.600	0.750	0.600
u	-0.333	-0.333	-1	-1	-1	-1

Latent heat in the discharge is explicitly excluded (VDI 3782 part 3 1985).

Sedimentation, dry and wet deposition

The sedimentation of particulate matter is realized by numerical particles with an additional velocity $\vec{v}_{add}$ in the transport Eq. 33. Sedimentation velocities used by ARTM depend on the aerodynamic diameter of particulate matter (VDI 3945 part 3 2000). The five size classes ARTM uses for particulate matter are given in Table 3 together with their sedimentation velocities.

Each numerical particle represents a mass and may carry an activity a_ν of a real particle species ν. If such a numerical particle hits an obstacle or the terrain surface, a fraction $\zeta_{\nu,dry}$ of its activity a_ν is deposited. After this process the new activity of the particle is given by

$$a_{\nu,new} = \left(1 - \zeta_{\nu,dry}\right) a_{\nu,old}. \tag{48}$$

The factor $\zeta_{\nu,dry}$ is given as

$$\zeta_{\nu,dry} = \frac{2 \, v_{dep}}{v_{dep} + v_{sed} + \sigma_{v,0} \sqrt{\frac{2}{\pi}} \, f_p} \tag{49}$$

Table 3 Size classes for particulate matter used in ARTM with their aerodynamic diameters d_{aero}, sedimentation velocities v_{sed}, deposition velocities v_{dep} and washout coefficients $r_{\nu,w}^0$ for a precipitation rate of 1 mm s^{-1} after Richter et al. (2015b)

Size class	d_{aero} in µm	v_{sed} in m s^{-1}	v_{dep} in m s^{-1}	$r_{\nu,w}^0$ in s^{-1}
PM 1	$d_{aero} < 2.5$	0.00	0.001	$1 \cdot 10^{-4}$
PM 2	$2.5 \leq d_{aero} < 10$	0.00	0.01	$2 \cdot 10^{-4}$
PM 3	$10 \leq d_{aero} \leq 50$	0.04	0.05	$3 \cdot 10^{-4}$
PM 4	$50 < d_{aero}$	0.15	0.20	$4 \cdot 10^{-4}$
PM u	$10 < d_{aero}$	0.06	0.07	$3 \cdot 10^{-4}$

where

$$f_p = \frac{\exp\left(-\frac{v_{sed}^2}{2\sigma_{v,0}^2}\right)}{1 + \operatorname{erf}\left(\frac{v_{sed}}{\sigma_{v,0}\sqrt{2}}\right)}, \tag{50}$$

$v_{dep/sed}$ is the deposition/sedimentation velocity given in Table 3 and $\sigma_{v,0}$ is the vertical wind fluctuation close to the ground (Janicke 1985; VDI 3945 part 3 2000). The deposition velocities for mercury and iodine in their organic bounded form are 0.0001 m s^{-1} and in their elementary form are 0.01 m s^{-1}, respectively. The particle is elastically reflected and its turbulent velocity is changed according to Eq. 38.

Wet deposition denotes the deposition due to washout by precipitation and thus also activity deposition occurs. For each particle species a specific washout coefficient $r_{\nu,w}^0$ is defined which is used to obtain the washout factor

$$r_{\nu,w} = r_{\nu,w}^0 \cdot \phi^a \tag{51}$$

where ϕ is the precipitation rate and a is a tracer specific exponent which may have (i) a value of $a = 0.8$ for particulate matter and iodine isotopes or (ii) a value of $a = 1$ for tritiated water (AVV 2012; Richter et al. 2015a). The activity fraction remaining in the atmosphere is given by

$$a_{\nu,new} = \left(1 - r_{\nu,w}\tau\right) a_{\nu,old} \tag{52}$$

(VDI 3945 part 3 2000).

The washout coefficients for the precipitation rate 1 mm h^{-1} of radionuclides as particulate matter are given in Table 3. Washout coefficients for organic bounded mercury and iodine are $7 \cdot 10^{-7}$ s^{-1}; in their elementary form, they are $7 \cdot 10^{-5}$ s^{-1}, respectively. The activity of a grid cell bottom area due to wet deposited originates from the vertical column above the bottom area to the top of the simulation domain (VDI 3945 part 3 2000).

Radioactive decay

The radioactive decay of numerical particles is represented as an exponential decay of the activity of a radioactive species as

$$a_{v,\text{new}} = a_{v,\text{old}} \cdot \exp\left(-\tau \lambda_{\text{decay}}\right) \tag{53}$$

where λ_{decay} is the decay constant for the corresponding radionuclide. Radioactive decay is only considered for numerical particles in the air not on the ground. Daughter products are not considered in ARTM (Richter et al. 2015a).

Activity concentration distribution

The simulation domain is divided into grid cells with coordinate indices i, j, k where the volume of a grid cell is denoted $V_{i,j,k}$.

The activity concentration of a particle species v consists of spatio-temporal mean activity concentration $\overline{a_{i,j,k}^{v}}$ within each grid cell and the time interval $[t_0, t_1]$. During this time interval, all numerical particles n with activity concentration $a_{v,n}$ contribute to the grid cell's mean activity concentration $\overline{a_{i,j,k}^{v}}$ for $n = 1 \ldots N$. N is the total particle number. Using the step function

$$f_{i,j,k}^{(n)}(t) = \begin{cases} 1 & \text{the particle } n \text{ is inside } V_{i,j,k} \text{ at time } t, \\ 0 & \text{otherwise} \end{cases} \tag{54}$$

for each numerical particle to decide at which time the particle contributes to the grid cell, the mean activity concentration can be calculated as

$$\overline{a_{i,j,k}^{v}} = \frac{\sum_{n=1}^{N} \int_{t_0}^{t_1} f_{i,j,k}^{(n)}(t) \cdot a_{v,n}(t) \, dt}{V_{i,j,k} \cdot (t_1 - t_0)} \tag{55}$$

(VDI 3945 part 3 2000).

Activity deposition rate distribution

The calculation of the dry activity deposition rate is similar to the calculation of the activity concentration distribution. The grid cells divide the terrain surface into areas $A_{l,m}$ where l and m identify the grid cells in x- and y-direction. At a certain point in time $t_{l,m}^{(n)}$ the particle n hits the terrain surface area $A_{l,m}$ and deposits a fraction $\zeta_{v,\text{dry}}$ of its activity. Thus, for a time interval $[t_0, t_1]$ the dry deposition rate is calculated as

$$\overline{d_{l,m}^{v}} = \frac{\sum_{n=1}^{N} \int_{t_0}^{t_1} \delta(t - t_{l,m}^{(n)}) \cdot \zeta_{v,\text{dry}} \cdot a_{v,n}(t) \, dt}{A_{l,m} \cdot (t_1 - t_0)} \tag{56}$$

(VDI 3945 part 3 2000).

γ-cloud shine

Radioactive isotopes — as part of the exhaust plume — may radiate γ-rays to all directions in space (Hallenbeck 1994). The γ-radiation of the plume at the terrain surface is called γ-cloud shine and is calculated by ARTM based on the grid cells (Richter et al. 2015a). The γ-radiation $G(x_{\text{lm}}, y_{\text{lm}})$ to the area of a grid cell at the surface with coordinates l and m is given as

$$G(x_{\text{lm}}, y_{\text{lm}}) =$$
$$\sum_{i,j,k} \overline{a_{i,j,k}^{v}} \int_{V_{i,j,k}} \frac{B(\mu R_{l,m}^{i,j,k}) K(\mu z, \mu S_{l,m}^{i,j,k}) \exp(-\mu R_{l,m}^{i,j,k})}{4\pi R_{l,m}^{i,j,k}{}^2} \, dx \, dy \, dz \tag{57}$$

where B is the dose buildup factor, μ is the aggregate attenuation coefficient, K is the correction factor for influences of the ground, S is the horizontal distance from the source of the γ-ray to the observed grid cell and R is the three-dimensional distance, respectively (VDI 3945 part 3 2000; Richter et al. 2015a).

The dose buildup factor B depends on the radiation energy. For simplicity, the energy spectrum is divided into two parts at 0.2 MeV. Energies of the lower (upper) part of the spectrum are approximated with coefficients for $E = 0.1$ MeV ($E = 1$ MeV), respectively (Richter et al. 2015a). Thus, the dose buildup factor is approximated as

$$B_E(\mu_E \cdot R) = 1 + \sum_{f=1}^{5} b_{E;f} \cdot (\mu_E \cdot R)^f \quad \text{for } E \in \{0.1 \text{ MeV}, 1 \text{ MeV}\} \tag{58}$$

with the aggregate attenuation coefficients $\mu_{1\,\text{MeV}} = 7.78 \cdot 10^{-3} \text{ m}^{-1}$ (AVV 2012; Richter et al. 2015a) and $\mu_{0.1\,\text{MeV}} = 1.82 \cdot 10^{-2} \text{ m}^{-1}$ (Jacob et al. 1984; Richter et al. 2015a). Values for the coefficients $b_{E;f}$ are summarized in Table 4. The coefficients $b_{1\,\text{MeV};f}$ are only valid if $\mu_{1\,\text{MeV}} \cdot R < 15$, for higher values $B_{1\,\text{MeV}}(\mu_{1\,\text{MeV}} \cdot R \geq 15) = B_{1\,\text{MeV}}(15)$ is used (AVV 2012; Richter et al. 2015a).

The correction coefficient for the influence of the ground K is approximated as

$$K_E(\mu_E \cdot z, \mu_E \cdot S) \approx \sum_{f=0}^{3} \sum_{g=0}^{3} a_{f,g} (\mu_E \cdot z)^f \cdot \exp\left(-\frac{g}{2} \cdot \mu_E \cdot S\right)$$
$$\text{for } E \in \{0.1 \text{ MeV}, 1 \text{ MeV}\} \tag{59}$$

where the coefficient $a_{f,g}$ is taken from Table 5 (Jacob and Paretzke 1985; Richter et al. 2015a; AVV 2012).

For the calculation of the γ-cloud shine, the integration of Eq. 57 is solved using Gaussian Quadratures (Press et al. 2002; Richter et al. 2015a). The calculation is straightforward for all grid cells except for the case where the grid cell of radiance also contains emitters. In that case, a coordinate transformation to polar coordinates is necessary in order to omit a singularity in the integrand of Eq. 57.

Details about the calculation are given by Richter et al. (2015a).

Table 4 Coefficients $b_{E;f}$ for the calculation of the dose buildup factors in Eq. 58 after Richter et al. (2015a) for energies of 0.1 MeV and after AVV (2012) for energies of 1 MeV

Energy	$f=1$	$f=2$	$f=3$	$f=4$	$f=5$
0.1 MeV	1.92	1.74	$-3.39 \cdot 10^{-2}$	$3.86 \cdot 10^{-2}$	$-2.11 \cdot 10^{-3}$
1 MeV	$7.7 \cdot 10^{-1}$	$3.5 \cdot 10^{-1}$	$-4.0 \cdot 10^{-2}$	$3.2 \cdot 10^{-3}$	$-8.2 \cdot 10^{-5}$

Sample error

Due to the statistical character of the particle transport, the activity and thus the concentration and deposition flux of each grid cell has a statistical uncertainty. This statistical uncertainty is estimated by the standard deviation of the mean (Janicke 2014). ARTM divides the numerical particles into N_g sub-groups. In a given time period h (e.g. 1 h), these particle sub-groups result in activity values $x_{h,n}$ with $n = 1 \ldots N_g$ for a grid cell. The sum over all groups is

$$s_h = \sum_{n=1}^{N_g} x_{h,n} \tag{60}$$

where an estimate of this sum can also be given as

$$X_{h,n} = N_g \cdot x_{h,n} \tag{61}$$

for each group member. The mean value of these N_g estimates $X_{h,n}$ is

$$M_h = \frac{1}{N_g} \sum_{n=1}^{N_g} X_{h,n}. \tag{62}$$

Table 5 Coefficients $a_{f,g}$ for the calculation of the correction coefficients for the influence of the ground K_E after Jacob and Paretzke (1985)

	0.1 MeV			
	$g=0$	$g=1$	$g=2$	$g=3$
$f=0$	0.279	0.595	-0.205	0.622
$f=1$	0.135	0.866	-0.716	-0.578
$f=2$	-0.0131	-0.324	0.1103	0.2892
$f=3$	0.0003	0.0313	-0.0017	-0.0337
	1 MeV			
	$g=0$	$g=1$	$g=2$	$g=3$
$f=0$	0.485	0.064	1.705	-1.179
$f=1$	0.137	1.878	-4.817	2.883
$f=2$	-0.0035	-0.8569	2.0527	-1.2552
$f=3$	-0.0018	0.0997	-0.2392	0.1503

The deviation of M_h from its expected value (M_h is the expected value for infinitely many numerical particles) is given by the mean squared error (variance) divided by N_g as

$$\frac{Var(X_{h,n})}{N_g} = \frac{1}{N_g(N_g - 1)} \sum_{n=1}^{N_g} (X_{h,n} - M_h)^2 = \frac{1}{N_g - 1} \left(N_g q_h - s_h^2 \right) \tag{63}$$

where q_h is the sum of squared activities

$$q_h = \sum_{n=1}^{N_g} x_{h,n}^2 \tag{64}$$

(Janicke 2022). For two sequential time periods h and $h+1$ the activity is given as

$$s_{h+(h+1)} = s_h + s_{h+1} \tag{65}$$

and the variances can be added because of the independent activity estimates (Press et al. 2002) as

$$\frac{Var(X_{h+(h+1),n})}{N_g} = \frac{Var(X_{h,n})}{N_g} + \frac{Var(X_{h+1,n})}{N_g}$$

$$= \frac{1}{N_g - 1} \left(N_g q_{h+(h+1)} - s_{h+(h+1)}^2 \right) \tag{66}$$

with

$$q_{h+(h+1)} = q_h + q_{h+1} + \frac{2}{N_g} s_h s_{h+1}. \tag{67}$$

For long simulation periods $H = h + (h + 1) + (h + 2) + \ldots$, ARTM uses Eqs. 65 and 67 iteratively to estimate the relative standard deviation of the mean activity as

$$\sqrt{\frac{Var(X_{H,n})}{s_H^2 N_g}} = \sqrt{\left(N_g \frac{q_H}{s_H^2} - 1 \right) \frac{1}{N_g - 1}} \tag{68}$$

(GRS 2015).

This sample error depends on the amount of numerical particles and decreases with increasing particle number. It can be seen as a figure-of-merit whether the number of numerical particles used in the simulation is large enough to obtain statistically reliable simulation results for the individual grid cells.

Sensitivity analysis setup

In order to analyse the sensitivity of model results on the different parameters, simulations of gas phase and particle-bound radioactive tracers are performed, released from a

single point source close to the left border of a rectangular simulation domain extending 10 000 m from west to east and 1 500 m from north to south. The vertical extension of the simulation domain is 1 500 m. The resolution for both horizontal directions is 50 m and the domain is divided into 19 horizontal levels stacked vertically with gradually growing thickness. The thicknesses of the different levels are summarized in Table 6. The terrain is modelled as a flat surface.

The simulated time period is 24 h with a constant and continuous emission rate from the source of 1 Bq s^{-1} of a radioactive tracer in the gas phase. Additional simulations are performed for PM, in which case the emitted activity rate stays unchanged but the emission only occurs in the first 20 h of the day. Doing so, all emitted particles are able to leave the simulation domain within 24 h which ensures the investigation of the fraction of particles being deposited relative to the emitted ones. The source is located at the horizontal coordinates (25 m, 25 m). The horizontal geometry can be seen in Fig. 1. Plume rise is not taken into account. For emissions in the gas phase the krypton isotope ^{85}Kr with decay constant $\lambda_{decay} = 2.05 \cdot 10^{-9}$ s^{-1} is used resulting in a decay ratio of less than 0.02% within 24 h. For the emission of PM, the cesium isotope ^{137}Cs with the decay constant $\lambda_{decay} = 7.32 \cdot 10^{-10}$ s^{-1} is used. The decay ratio is less than 0.006% within 24 h. Therefore, the radioactive decay has no significant effect on the simulation results in this study.

Table 6 Default setup of the horizontal levels in ARTM. The height of a level AGL and the level thickness are given in metre. After Richter et al. (2015b)

Level	Height of level AGL in m	Thickness in m
19	1200	300
18	1000	200
17	800	200
16	700	100
15	600	100
14	500	100
13	400	100
12	300	100
11	200	100
10	150	50
9	100	50
8	65	35
7	40	25
6	25	15
5	16	9
4	10	6
3	6	4
2	3	3
1	0	3

A default set of input parameters is defined including a wind speed of 1 m s^{-1}, a wind direction of 270° (westerly wind), a roughness length of $z_0 = 0.5$ m, a factor $d = 6$ of the zero plane displacement $d_0 = d \cdot z_0$, a source height of $h_s = 20$ m and a neutral DC. The default values are marked with (*) in Table 7.

The sensitivity analysis is performed in a "local" manner around the default set of input parameters, i.e. one input parameter is varied at a time while all other parameters are held constant. In this study the effects of the DC, the roughness length z_0, the factor d of the zero plane displacement, the source height above ground level and the tracer type which is either a tracer in the gas phase or PM with four different size classes representing different aerodynamic diameters d_{aero} are analysed systematically. The values of the possible input parameters are given in Table 7. For some input parameters also cross interactions with other parameters (e.g. DC and z_0, or DC and tracer type) are investigated. An example for the average deposition rate within the simulation domain is given in Fig. 1.

The sensitivity is quantified by analysing the impact on the following three main characteristics of the simulated three-dimensional plume: (i) the plume volume and its three-dimensional spread; (ii) the position of maximum activity concentration (PMAC) for each horizontal simulation level; and (iii) the activity deposition of particulate matter.

As a quantity describing the spread of the exhaust plume, the normalized volume covered by the pollutant is used. The normalization can be done either by normalizing the volume covered by the plume in one horizontal level with the entire volume of that specific level or by normalizing the volume covered by the whole plume in the simulation domain with the volume of the simulation domain. Furthermore, the mean plume volume of the three lowest simulation levels is determined to get information about the spread close to the ground.

The PMAC in each horizontal level is described by the horizontal distance between the location of the maximum concentration and the source in x-direction x_{max}. To compare the influence of the input parameters on the concentration distribution close to the ground, the slope of the maximum concentration distribution given by

$$m_{slope} = \frac{h_s - h_l}{x_{max}} \tag{69}$$

is calculated, where h_s is the source height and h_l is the level height. These slopes are only used for comparison when the investigated levels are below the source level.

For the analysis of the activity deposition rate, the surface area of the simulation domain is divided into rings formed by concentric circles around the source. The

Fig. 1 Simulation domain with the average activity deposition rate of PM 1 in logarithmic scale. The red lines denote the concentric circles around the source dividing the ground surface into evaluation areas. The x-direction is in west-east orientation, the y-direction in north-south orientation
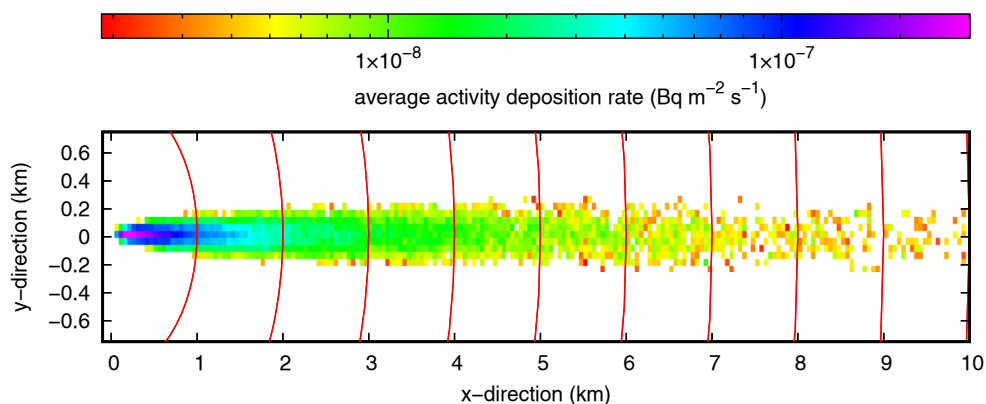
distance between the circumferences is 1 km as depicted in Fig. 1. The deposition rate is evaluated in each ring and for each particle size class, respectively. Additionally, the total amount of deposited activity for the different particle size classes is evaluated.

All the modelled concentration and deposition rate values are the result of a statistical process (random turbulent velocity). Thus, each concentration value or deposition rate is subject to a sampling error (compare "Sample error"). A high sampling error of a grid cell indicates the concentration (deposition rate) value to be rather random. This is the case for the grid cells at the edge of the plume. For this analysis, the simulation results are limited to those concentration values and deposition rates having a maximum sampling error of 30% assuring a sufficient statistical significance of the result.

Results and discussion

Volume of the exhaust plume

The volume of the exhaust plume in the simulation domain — and for each level separately — gives insights into how the plume spreads in all three dimensions. The diffusion categories have a strong impact on the plume volume as shown in Fig. 2 where the volume covered by the plume in each horizontal level is normalized by the level volume, respectively, for all the different diffusion categories. It can be seen that the overall plume volume increases with decreasing atmospheric stability. The plume volume of the diffusion category "very stable" (smallest plume spread) covers only 1% of the volume of the entire simulation domain while the plume with the biggest spread ("very unstable") reaches 71% (see Table 8). However, the normalized volume in the lowest three levels does not show a monotonic behaviour. For these levels, the largest mean plume level volume is found for neutral boundary layer conditions (37.3 %) while the smallest mean plume level volume is found for very unstable conditions (13.3 %) resulting in a variation of the mean plume volume of the lowest three levels of 24%.

For levels above the emission source level (level 5) the volume increases with atmospheric instability. Especially the extent of the plume towards higher levels is clearly observable in Fig. 2. This vertical spread is not limited by the simulated mixing layer height as it is shown in Table 8. For neutral atmospheric conditions the mixing layer height is above the top level of the plume while for all other cases it is directly at the lower border of the top plume level (for indifferent stratification), within the top plume level ("stable" and "very stable") or below the lower border of the top plume level ("unstable" and "very unstable").

Table 7 Input parameters and ranges of the investigated input parameters of ARTM. The values marked with * are part of the default parameter set

Input parameter	Values
Diffusion category DC	very stable, stable, neutral*, indifferent, unstable, very unstable
Roughness length z_0	0.1 m, 0.2 m, 0.5 m*, 1.0 m, 1.5 m, 2.0 m
Zero plane displacement factor d	3, 6*, 9, 15
Source height h_s	10 m, 20 m*, 50 m, 75 m, 80 m, 85 m, 110 m, 120 m
Tracer type	Gas*, PM 1, PM 2, PM 3, PM 4

Fig. 2 Normalized plume volume of the 19 horizontal levels for the diffusion categories. The point source is located at 20 m AGL (in level 5)
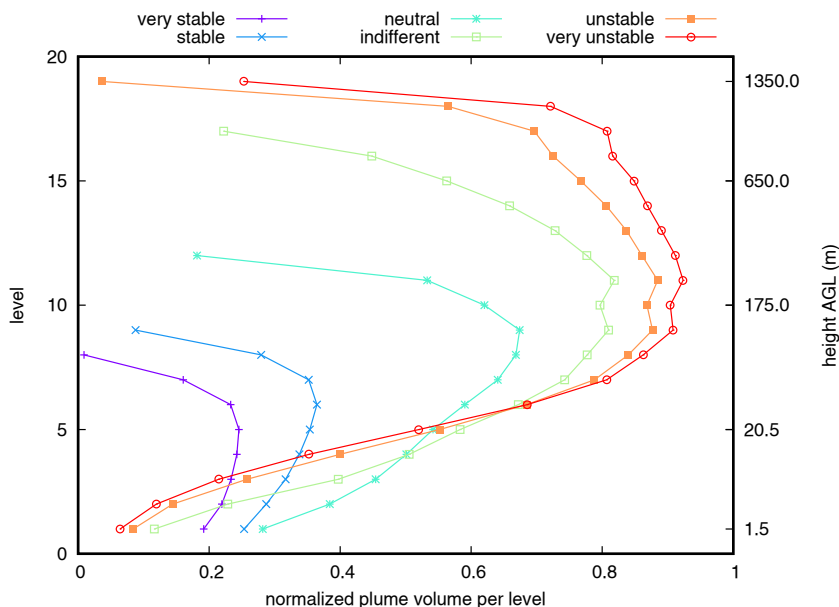
The roughness length has less influence on the plume volume with a minimum coverage of 7% for $z_0 = 0.1$ m of the simulation domain and a maximum coverage of 24% for $z_0 = 2.0$ m while keeping the other input parameters' default values. In the lowest three simulation levels, only a very weak volume alternation (5.3%) can be observed. No spread towards higher levels is observed; thus, growth of the plume coverage from small to large values of z_0 occurs in the mid levels of the plume. However, the influence of z_0 on the plume volume depends strongly on the diffusion category. The maximum effect of z_0 on the volume is observed for neutral atmospheric conditions. For both more stable and less stable conditions, the influence of the roughness length on the plume volume decreases.

The overall influence of the zero plane displacement height d_0 on the plume volume is weaker than the influence caused by the roughness length. Nevertheless, the mean plume volume for the three lowest simulation levels shows a different picture with a variation of 7% by varying the zero plane displacement factor as given in Table 7. This shows

a stronger influence of d_0 on the lowest three simulation levels than z_0. The turbulence is determined by the Obukhov length and thus the friction velocity u_* via DC and z_0 while d_0 predominantly influences the wind profile because it shifts the logarithmic wind profile vertically. There is no spread of the plume towards higher levels observed by varying the zero plane displacement.

The overall volume of the plume is hardly affected by a variation of the source height in the given range. However, the source height strongly influences the particle spread in the lowest three levels. When varying the source height the mean plume volume of the lowest three levels changes by 9.8%. In agreement with the boundary layer model the diffusion coefficient close to the ground is smaller than for higher levels. Therefore, tracers do not spread well at levels close to the ground. A spread of the plume towards higher levels is expected to be proportional to the source height but was not observed because of the limited range of the source height variation compared to the simulation grid resolution in medium and high levels.

Distance from source to maximum concentration

The turbulence in the atmosphere is not only a key to the plume extent but also influences the PMAC in each horizontal level of the plume. Figure 3 shows that the distance between the source and the PMAC decreases with increasing turbulence in the atmosphere. The information about the position of the maximum concentration is of special interest in the levels close to the ground where most organisms are living. For the lowest three levels average slopes for the PMAC from -13.1 m km^{-1} to -128.7 m km^{-1} for very stable and very unstable

Table 8 The plume volume relative to the volume of the simulation domain, the mixing layer height and the upper and lower boarder of the top plume level for the different diffusion categories DC

DC	Plume volume	Mixing layer height	Top plume level
very unstable	71%	1100 m	1200–1500 m
unstable	61%	1100 m	1200–1500 m
indifferent	39%	800 m	800–1000 m
neutral (default)	13%	418 m	300–400 m
stable	2%	127 m	100–150 m
very stable	1%	62 m	60–100 m

Fig. 3 Position of the maximum concentration in each level for the six diffusion categories. The point source is located at a height of 20 m AGL (in level 5)
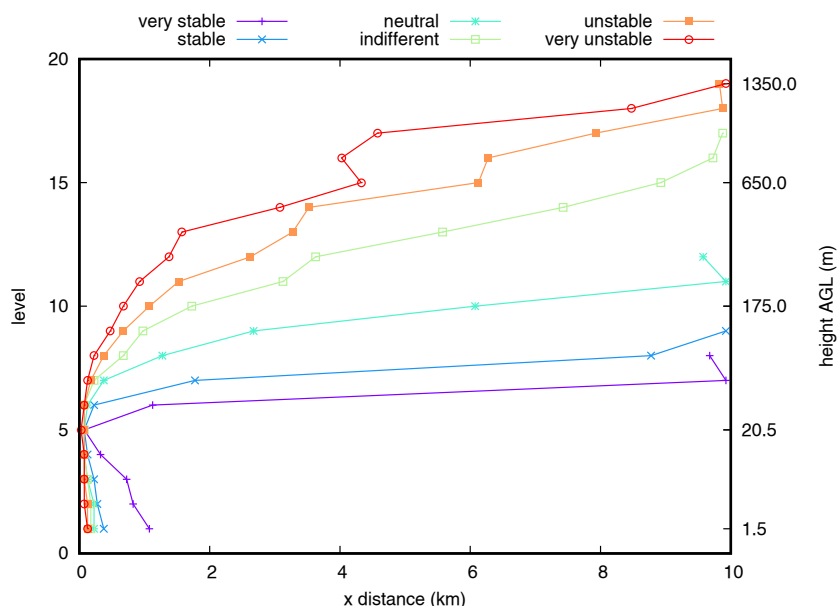
conditions were observed, respectively. This shows the very unstable atmosphere to be better mixed in the levels close to the ground despite the surface effects.

Compared to DC a variation of the roughness length has a weaker influence on the distance between the source and the PMAC. This is observed in the middle and upper levels but also in the levels close to the ground. Here, the slopes of the three lowest levels are steeper compared to those for a variation of DC and determined between -39.5 m km^{-1} and -153.3 m km^{-1}. This indicates the PMAC to be closer to the source than it is the case for the variation of the diffusion categories. However, there is a strong dependence of the diffusion category especially in the lowest levels. The

influence of the roughness length increases for more stable conditions while it decreases for more unstable conditions.

The zero plane displacement hardly affects the distance between source and the maximum concentration.

In contrary, the height of the source has a strong influence on the maximum concentration. With a shift of the source to different heights AGL, the plume and thus the PMAC in each level shift vertically as well.

Deposition of PM on the ground

Particulate matter can be deposited to the ground. Depending on the aerodynamic diameter the deposition rate changes

Fig. 4 Normalized activity deposition rate at different distances from the source for the four different particulate matter size classes. The activity deposition rates are shown for very stable, neutral (default) and very unstable boundary layer conditions
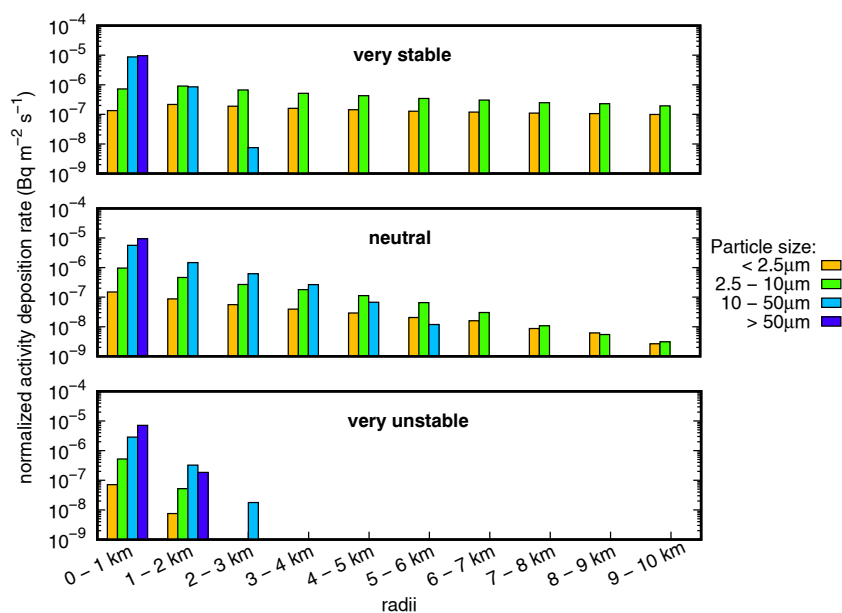
Table 9 Fractions of deposited activity per diffusion category DC and particle size class in the whole simulation domain

DC	Deposition (%)			
	PM 1	PM 2	PM 3	PM 4
very unstable	0.8	6.0	33.2	75.5
unstable	1.3	8.7	47.7	88.6
indifferent	2.0	12.2	61.8	94.5
neutral (default)	4.3	21.8	83.8	98.4
stable	9.8	40.7	97.3	99.7
very stable	14.6	47.3	99,5	99.9

as it can be seen in Fig. 4 for neutral conditions (default) as well as for very stable and very unstable atmospheric conditions. For neutral conditions, deposition rates are larger for large particles resulting in a bigger amount of deposited material closer to the source. While for PM larger than 10 μm (PM 3 and PM 4) almost all particles are deposited, smaller particles can spread widely and can stay in the atmosphere for a long time. Values of the deposited activity fractions are given in Table 9.

The deposition rate is dependent not only on the aerodynamic diameter but also on the diffusion category. In Fig. 4 the dependence of DC can also be observed. In the case of very stable atmospheric conditions the deposition rate for PM smaller than 10 μm (PM 1 and PM 2) decreases only slightly with increasing distance from the source while the larger particles are almost completely deposited after 3 km (99.46% of particles of 10–50 μm and 99.93% of particles > 50 μm). With increasing turbulence in the atmosphere the overall deposition rate decreases. This leads to a wider spread of the larger particles at neutral atmospheric conditions and thus to less particles deposited to the ground at very unstable conditions. This is explained by the turbulence in the atmosphere cancelling out the sedimentation and keeps the particles in the atmosphere. This can also be seen in Table 9 where the amount of deposited activity shows the lowest values at very unstable conditions for all particle sizes and monotonically increase when the atmosphere becomes less turbulent.

Conclusion

The present work gives a extensive description of the Atmospheric Radionuclide Transport Model including the wind field model, the transport model and the treatment of tracers both in the gas phase and PM as well as the calculation of activity concentration values, dry deposition

rates and their estimated statistical error. A sensitivity analysis was performed, which gives insight into how the simulation results change with respect to changes in the input parameters around the specified location (default input parameters) in the input parameter space.

The diffusion category was found to be the most influencing parameter for the 3-dimensional spread of tracers in the simulation domain followed by the roughness length. Other parameters show significantly weaker effects. Both the DC and the roughness length determine the Obukhov length and thus have a strong effect on the friction velocity, the turbulent fluctuation and the mixing in the atmosphere. When focusing on the spread of tracers near the ground, the zero plane displacement and the source height have a larger influence than the roughness length. Due to the boundary layer effects at the interface between the atmosphere and the ground, the turbulence becomes weaker in the levels close to the ground. This reduces the effect of the DC and the roughness length. The zero plane displacement, in contrast, changes the wind profile and therefore modifies the reducing character of the ground while the source height shifts the plume vertically.

The turbulence in the atmosphere is also the dominant parameter that controls the PMAC in the different horizontal levels but its influence decreases for the levels close to the ground. This is in agreement with the atmosphere-surface interaction effect. Besides this, the source height controls the vertical positions of the PMAC. The roughness length and the zero plane displacement factor hardly affect the PMAC in neutral (default) conditions but it shows that the effect of the roughness length strongly depends on the atmospheric conditions. The degree of dependence originates from ARTM's internal DC-roughness length Table (Table 1) which is used to determine the Obuhkov length.

The amount of deposited particles depends on the particle size and on the atmospheric stability, i.e. with increasing stability and decreasing particle size the flight time increases. Furthermore, the stability of the atmosphere controls the ability to keep PM in the atmosphere and counteracts sedimentation.

The obtained results of the local sensitivity analysis reveal the prominent role of the DC for the activity concentration and deposition rate distribution. This shows the importance of an accurate determination of the DC for any simulation attempt since inaccuracies may change the simulation result tremendously. For the roughness length, the zero plane displacement and the source height no clear importance ranking can be given. Additional investigations such as global sensitivity analysis methods are necessary to get a more complete information about the importance of the input parameters. Furthermore, a validation with

three-dimensional measurements such as observational data from measurement towers or airborne measurements is necessary to validate the observed structure of the dispersion not only at ground level but at higher levels within the boundary layer. Nevertheless, the presented sensitivity analysis may help users of ARTM to better understand the model, interpret simulation results and guide further modelling attempts.

Data availability The datasets generated during and/or analysed during the current study are available from the corresponding author on reasonable request.

Software availability The software ARTM is freely available and provided by the Federal Office for Radiation Protection of Germany under https://www.bfs.de/EN/topics/ion/environment/air-soil/emission-monitoring/artm.html.

Declarations

Consent to participate All authors declare consent to participate in this article.

Consent to publication All authors declare consent to publish this article.

Conflict of interest The authors declare no competing interests.

References

AVV (2012) Allgemeine Verwaltungsvorschrift zu §47 Strahlenschutzverordnung: Ermittlung der Strahlenexposition durch die Ableitung radioaktiver Stoffe aus kerntechnischen Anlagen oder Einrichtungen. Bundesanzeiger Verlagsgesellschaft mbH, Bundesministerium für Umwelt, Naturschutz und Reaktorsicherheit. http://dipbt.bundestag.de/dip21/brd/2012/0088-12.pdf

AVV Tätigkeiten (2020) Allgemeine Verwaltungsvorschrift zur Ermittlung der Exposition von Einzelpersonen der Bevölkerung durch genehmigungs- oder anzeigebedürftige Tätigkeiten (AVV Tätigkeiten). Bundesanzeiger Verlagsgesellschaft mbH, Bundesministerium für Umwelt, Naturschutz und nukleare Sicherheit. http://www.verwaltungsvorschriften-im-internet.de/bsvwvbund_08062020_SII51148301.htm

Briggs GA (1971) ME 8E - Some Recent Analysis of Plume Rise Observasion. In: Englund HM, Beery WT (eds) Proceedings of the Second International Clean Air Congress. Academic Press, pp 1029–1032

Gal-Chen T, Somerville RCJ (1975) On the use of a coordinate transformation for the solution of the Navier-Stokes equations. J Comput Phys 17(2):209–228. https://doi.org/10.1016/0021-9991(75)90037-6

GRS (2007) Entwicklung, Validierung und Bereitstellung eines Atmosphärischen Ausbreitungsmodells für Luftgetragene Radioaktive Stoffe der Basis des Ausbreitungsmodells AUSTAL 2000 der neuen TA Luft. Bundesministerium für Umwelt, Naturschutz und Reaktorsicherheit, Bonn. https://www.bmu.de/fileadmin/bmu-import/files/pdfs/allgemein/application/pdf/schriftenreihe_rs710.pdf

GRS (2015) ARTM - Atmospheric Radionuclid-Transport-Model Version 2.8.0. (Source Code)

Hallenbeck WH (1994) Radiation Protection. CRC Press, Boca Raton

Hamby DM (1994) A review of techniques for parameter sensitivity analysis of environmental models. Environ Monit Assess 32(2):135–154. https://doi.org/10.1007/BF00547132

Hettrich S (2017) Validation and verification of the atmospheric radionuclide transport model (ARTM). Ph.D. Thesis, Ludwig Maximilians Universität München. https://edoc.ub.uni-muenchen.de/20914/1/Hettrich_Sebastian.pdf. Accessed: February 25th 2022

Homicz GF (2002) Three-dimensional wind filed modeling: a review. Technical report, Sandia National Laboratories. https://doi.org/10.2172/801406

Jacob P, Paretzke HG (1985) Air-ground interface correction factors for gamma emitters in air. Health Phys 48(2):183–191. https://doi.org/10.1097/00004032-198502000-00005

Jacob P, Paretzke HG, Wölfel J (1984) Monte Carlo Calculation and Analytical Approximation of Gamma-Ray Buildup Factors in Air. Nucl Sci Eng 88(2):113–122. https://doi.org/10.13182/NSE84-A28405

Janicke (2014) Austal2000 - Programmbeschreibung zu Version 2.6. Umweltbundesamt

Janicke (2015) TALdia - Diagnostic Wind Field Model Version 2.2.2. (Source Code)

Janicke L (1985) Particle Simulation of Dust Transport and Deposition and Comparison with Conventional Models. In: De Wispelaere C (ed) Air Pollution Modeling and Its Application IV. Springer US, Boston, pp 759–769. https://doi.org/10.1007/978-1-4613-2455-3_41

Janicke L (2000) A random walk model for turbulent diffusion. Technical report, Janicke Consulting. http://www.janicke.de/data/bzu/bzu-001-01.pdf

Janicke L, Janicke U (2003) Entwicklung eines modellgestützen Beurteilungssystems für den anlagenbezogenen Immissionsschutz.

Janicke Consulting. https://www.umweltbundesamt.de/sites/default/files/medien/2338/dokumente/a2k-1.0.6-report_de.pdf

Janicke U (2022) Statistical Uncertainty Estimated by AUSTAL2000. (Personal Communication)

Janicke U, Janicke L (2004) Weiterentwicklung eines diagnostischen Windfeldmodells für den anlagenbezogenen Immissionsschutz (TA Luft). Technical report no. UBA-FB000842, Janicke Consulting

Kleijnen JPC (1995) Verification and validation of simulation models. Eur J Oper Res 82(1):145–162. https://doi.org/10.1016/0377-2217(94)00016-6

Klug W (1969) Ein verfahren zur bestimmung der ausbreitungsbedingungen aus synoptischen beobachtungen. Staub Reinhaltung Luft 29(4):143–147

Lamb RG, Hogo H, Reid LE (1979) A Lagrangian Approach to Modeling Air Pollutant Dispersion: Development and Testing in the Vicinity of a Roadway. Technical report. PB-296095 United States NTIS, PC A06/MF A01. HEDB English. Systems Applications, Inc., San Rafael

Lee U, Lee C, Kim M, Kim HR (2019) Analysis of the influence of nuclear facilities on environmental radiation by monitoring the highest nuclear power plant density region. Nucl Eng Technol 51(6):1626–1632. https://doi.org/10.1016/j.net.2019.04.007

Leelőssy A, Molnár F, Izsák F, Havasi A, Lagzi I, Mészáros R (2014) Dispersion modeling of air pollutants in the atmosphere: a review. Open Geosci 6(3):257–278. https://doi.org/10.2478/s13533-012-0188-6

Maronga B, Gryschka M, Heinze R, Hoffmann F, Kanani-Sühring F, Keck M, Ketelsen K, Letzel MO, Sühring M, Raasch S (2015) The Parallelized Large-Eddy Simulation Model (PALM) version 4.0 for atmospheric and oceanic flows: model formulation, recent developments, and future perspectives. Geosci Model Dev 8(8):2515–2551. https://doi.org/10.5194/gmd-8-2515-2015

Martens R, Bruecher W, Richter C, Sentuc F, Sogalla M, Thielen H (2012) Erweiterung und Validierung von ARTM für den Einsatz als Ausbreitungsmodell in AVV und SBG. Techincal report, Gesellschaft für Anlagen- und Reaktorsicherheit mbH (GRS), Koeln

Maryon RH, Smith FB, Conway BJ, Goddard DM (1991) The U.K. nuclear accident model. Prog Nucl Energy 26(2):85–104. https://doi.org/10.1016/0149-1970(91)90043-O

Mayall A (2003) Modelling the dispersion of radionuclides in the atmosphere. In: Marian Scott E (ed) Modelling Radioactivity in the Environment. 1st edn., vol 4. Elsevier, pp 13–54

Mesinger F, Arakawa A (1976) Numerical methods used in atmospheric models. Technical report, World Meteorological Organization. https://oceanrep.geomar.de/40278/1/Mesinger_ArakawaGARP.pdf

Moses H, Carson JE (1968) Stack design parameters influencing plume rise. J Air Pollut Control Assoc 18(7):454–457. https://doi.org/10.1080/00022470.1968.10469155

Moussafir J, Oldrini O, Tinarelli G, Sontowski J, Dougherty CM (2004) A new operational approach to deal with dispersion around obstacles: the MSS (Micro Swift Spray) Software Suite. In: 9th Int. Conf. on Harmonisation within Atmospheric Dispersion Modelling for Regulatory Purposes. https://harmo.org/Conferences/Proceedings/_Garmisch-Partenkirchen/publishedSections/5.26.pdf

Nuclear Safety Standards Commission (KTA) (2017) Instrumentation for Determining the Dispersion of Radioactive Substances in the Atmosphere (Technical report). http://www.kta-gs.de/e/standards/1500/1508_engl_2017_11.pdf

Oldrini O, Armand P, Duchenne C, Olry C, Moussafir J, Tinarelli G (2017) Description and preliminary validation of the PMSS fast response parallel atmospheric flow and dispersion solver in complex built-up areas. Env Fluid Mech 17(5):997–1014. https://doi.org/10.1007/s10652-017-9532-1

Press WH, Teukolsky SA, Vetterling WT, Flannery BP (2002) Numerical recipes in C: the art of scientific computing, 2nd edn. Cambridge University Press

Rao KS (2005) Uncertainty Analysis in Atmospheric Dispersion Modeling. Pure Appl Geophys 162(10):1893–1917. https://doi.org/10.1007/s00024-005-2697-4

Ratto CF (1996) An overview of mass-consistent models. In: Lalas DP, Ratto CF (eds) Modelling of Atmospheric Flow Fields. World Scientific Publishing Co Pte Ltd, Singapore, pp 379–400

Ratto CF, Festa R, Romeo C, Frumento OA, Galluzzi M (1994) Mass-consistent models for wind fields over complex terrain: The state of the art. Environ Softw 9(4):247–268. https://doi.org/10.1016/0266-9838(94)90023-X

Richter C (2016) State of the art atmospheric dispersion modelling: should the Gaussian plume model still be used? Kerntechnik 81(5):559–564. https://doi.org/10.3139/124.110727

Richter C, Sogalla M, Thielen H, Martens R (2015a) ARTM Atmosphärisches Radionuklid-Transport-Modell mit Radon Prozessor und SBG-Modul

Richter C, Sogalla M, Thielen H, Martens R (2015b) Atmosphärisches Radionuklid-Transport-Modell mit der graphischen Benutzeroberfläche GO-ARTM

Sasaki Y (1958) An Objective Analysis Based on the Variational Method. J Meteorol Soc Jpn Ser II 36(3):77–88. https://doi.org/10.2151/jmsj1923.36.3_77

Sasaki Y (1970) Some Basic Formalisms in Numerical Variational Analysis. Mon Weather Rev 98(12):875–883. https://journals.ametsoc.org/view/journals/mwre/98/12/1520-0493_1970_098_0875_sbfinv_2_3_co_2.xml

Seinfeld JH (1986) Atmospheric chemistry and physics of air pollution. Wiley, New York

Sherman CA (1978) A mass-consistent model for wind fields over complex terrain. J Appl Meteorol Climatol 17(3):312–319

Simmonds JR, Lawson G, Mayall A (1995) Methodology for assessing the radiological consequences of routine releases of radionuclides to the environment. Techincal report, National Radiological Protection Board (UK). https://op.europa.eu/en/publication-detail/-/publication/1078584c-9e21-40d1-9104-82939f315f25

Stein AF, Draxler RR, Rolph GD, Stunder BJB, Cohen MD, Ngan F (2015) NOAA's HYSPLIT atmospheric transport and dispersion modeling system. Bull Am Meteorol Soc 96(12):2059–2077. https://doi.org/10.1175/BAMS-D-14-00110.1

Stohl A, Forster C, Frank A, Seibert P, Wotawa G (2005) Technical note: The Lagrangian particle dispersion model FLEXPART version 6.2. Atmos Chem Phys 5(9):2461–2474. https://doi.org/10.5194/acp-5-2461-2005

StrlSchV (2018) Verordnung zum Schutz vor der schädlichen Wirkung ionisierender Strahlung (Strahlenschutzverordnung - StrlSchV). http://www.gesetze-im-internet.de/strlschv_2018/StrlSchV.pdf

Stull RB (1988) An introduction to boundary layer meteorology, vol 13. Springer Science & Business Media

TA Luft (2002) Erste Allgemeine Verwaltungsvorschrift zum Bundes-Immissionsschutzgesetz (Technische Anleitung zur Reinhaltung der Luft - TA Luft), vol 25-29

VDI 3782 part 3 (1985) Determination of plume rise. Retrieved from https://www.beuth.de/de/technische-regel/vdi-3782-blatt-3/635897. VDI-Handbuch Reinhaltung der Luft, Band 1

VDI 3783 part 8 (2002) Turbulent parameters for dispersion models supported by measurement data. Retrieved from https://www.beuth.de/de/technische-regel/vdi-3783-blatt-8/59262605. VDI-Handbuch Reinhaltung der Luft, Band 1b

VDI 3945 part 3 (2000) Atmospheric dispersion models - Particle model. Retrieved from https://www.beuth.de/de/technische-regel/vdi-3945-blatt-3/36552631. VDI/DIN-Handbuch Reinhaltung der Luft, Band 1b

Walter H (2004) Comparison of results from dispersion models for regulatory purposes based on Gaussian-and Lagrangian-algorithms: an evaluating literature study. In: HARMO 9: 9. International Conference on Harmonisation within Atmospheric Dispersion Modelling for Regulatory Purposes, vol 1. Forschungszentrum Karlsruhe GmbH, pp 167–171. https://www.osti.gov/etdeweb/biblio/20538796